Estuarine suspended particulate matter concentrations from sun-synchronous satellite remote sensing: Tidal and meteorological effects and biases

Eleveld, M.A., Wal, D. van der, van Kessel, T.

Remote Sensing of Environment, 143, 204-215

Published version: http://dx.doi.org/10.1016/j.rse.2013.12.019

Estuarine suspended particulate matter concentrations from sun-synchronous satellite remote sensing: Tidal and meteorological effects and biases

Marieke A. Eleveld [a,*], Daphne van der Wal [b], Thijs van Kessel [c]

[a] Institute for Environmental Studies, VU University Amsterdam (VU-IVM), De Boelelaan 1087, 1081 HV, Amsterdam, the Netherlands
* Corresponding author. E-mail address: marieke.eleveld@vu.nl (M.A. Eleveld) tel. +31 (0)20 5989591; fax +31 (0)20 5989553
[b] NIOZ Royal Netherlands Institute for Sea Research, P.O. Box 140, 4400 AC, Yerseke, the Netherlands. daphne.van.der.wal@nioz.nl
[c] Department Marine and Coastal Systems, Deltares, P.O. Box 177, 2600 MH, Delft, the Netherlands. thijs.vankessel@deltares.nl

Highlights

- Remote sensing captures estuarine suspended particulate matter dynamics
- Composites enable appraisal of tidal and seasonal variation in SPM
- Westerschelde SPM is equally impacted by tidal and meteorological drivers
- Biases in SPM from optical sensors on sun-synchronous satellites are quantified
- Sampling bias for fair weather exceeds tidal aliasing effect at the mouth

Always cite this paper as

Eleveld, M.A., van der Wal, D., van Kessel, T., 2014. Estuarine suspended particulate matter concentrations from sun-synchronous satellite remote sensing: Tidal and meteorological effects and biases. Remote Sensing of Environment 143, 204-215. doi:10.1016/j.rse.2013.12.019. http://dx.doi.org/10.1016/j.rse.2013.12.019

Abstract

Optical data from a sun-synchronous satellite were used to investigate how large-scale estuarine suspended particulate matter (SPM) concentrations were affected by tidal and bulk meteorological drivers, and how retrieved SPM is biased by tidal aliasing and sampling under clear sky conditions. Local absorption and scattering properties were used to derive surface SPM maps from 84 cloud-free ENVISAT MERIS FR reflectance images of the Westerschelde estuary (51° 30' N, 3° 30' E) for the period 2006-2008, and validated with in situ SPM at fixed stations (r=0.89 for geometric means). The distinctly different SPM maps were categorized for different tidal and seasonal conditions. Resulting composites reveal spatial patterns in SPM as a function of semi-diurnal tidal phase, fortnightly tidal phase, or season. For the estuary proper, tidal and seasonal effects on the variation of SPM are similar in magnitude. Observed controls for surface SPM are distance to shallow source area, tidal current velocity, and advection of North Sea and estuarine surface waters. Turbidity maxima appear only during favourable tidal and meteorological conditions. For the Westerschelde, the bias introduced by sun-synchronous sampling causes low water image acquisitions to uniquely coincide with spring tides, and high water images with neap tides. Cloud-free images were associated with low wind velocities. Simulations from a mud transport model confirmed the overestimation of geometric mean SPM from the tidal aliasing, and underestimation from fair weather. This resulted in a net relative error of -8% at the wave-exposed mouth, but biases cancelled out in the upper estuary. We argue that local biases should be considered when interpreting water quality products for estuaries and coasts around the world.

Keywords total suspended matter; ocean colour; sun-synchronous overpass; tidal aliasing; seasonality; optical properties; Western Scheldt

1. Introduction

Estuaries are found along many of the world's diverse coastlines and provide many ecosystem services, ranking at the top in total monetary value per hectare per year (Costanza et al., 1997). They support important ecosystem functions, such as biogeochemical cycling and movement of nutrients, maintenance of biodiversity and biological production, and mitigation of floods (Meire et al., 2005). Variation in transport of fine sediments is at the heart of many of these functions, being a driver for primary production through nutrient cycling, a pressure on ecosystem state through light attenuation (Cloern, 1996; Gattuso et al., 1998), and a regulator of estuarine landscape and habitat development (Dyer, 1989; Van der Wal et al., 2010). Estuaries are complex environments in which dissolved and suspended particulate matter (SPM) discharged by rivers in upland basins are concentrated (Heip et al., 1995) and mixed with marine water and other substances (Middelburg and Nieuwenhuize, 1998). Suspended particulate matter (SPM) is here defined as all matter – organic and inorganic, including clay (< 2 μm), silt (2 - 63 μm), flocs, and occasionally sand – sampled in the top of the water column, which stays on a Whatman GF/F glass fibre filter with an approximate pore size of 0.7 μm (Eleveld et al., 2008).

The concentration of suspended material at the top of the water column has been quantified using detailed optical airborne and satellite remote sensing (Robinson et al., 1998; Uncles et al., 2001) and optical modelling with spectral properties of estuarine SPM (Bale et al., 1994; Forget et al., 1999), although these optical properties may change over the estuary (Mobley et al., 2004; Gallegos et al., 2005; Bowers et al., 2009; Blondeau-Patissier et al., 2009). The availability of dedicated ocean colour satellite sensors such as MERIS and MODIS, which are spectrally configured for the specific bio-optical properties of aquatic media has further stimulated the retrieval of suspended sediments in optically complex waters (i.e., waters that contain uncorrelated light absorbing substances) such as estuaries (Doerffer and Schiller, 2007; Nechad, 2010). Their extensive panoramas, which easily cover an entire estuary, and more frequent data acquisition revealed huge differences in retrieved SPM concentrations from different images (Miller and McKee, 2004; D'Sa et al., 2007; Van der Wal et al., 2010). Their interpretation remains cumbersome until regularities, such as periodicities are recognised. The emergent SPM patterns in the top of the water column can be expected to be a response to astronomical tidal, and seasonal meteorological drivers (tides, and wind and discharge) that lie behind resuspension, and estuarine transport processes such as estuarine circulation, tidal straining and wind-induced variations in vertical mixing and horizontal advection (Burchard et al., 2008; Van der Wal et al., 2010).

However, a number of biases likely occur in the estimation of SPM from satellite remote sensing. Firstly, the near-polar orbits of most satellites carrying dedicated ocean colour sensors such as MERIS are sun-synchronous. To systematically maximise solar elevation and mitigate sun-glint at image acquisition, overpasses are locked to the position of the sun, which also means that every orbit always crosses the equator at the same local solar time. Hence, the solar semi-diurnal *S2* tidal phase will be the same every time the satellite revisits the same location on the sea surface. The principle, lunar, semi-diurnal *M2* tides (low water, flood, high water and ebb) have a period of about 12 h and 25 min, which we often notice as semi-diurnal tides being a little later each next (solar) day. The phase difference between *M2* and *S2* also causes them to be in and out of phase every 14.8 days, creating spring (*M2*+*S2*) and neap (*M2*-*S2*) tides respectively (Sorensen, 2006). Consequently, the alignment of the sun and moon influences both phases and amplitudes of the tides at a certain location. Furthermore, the locking of overpass to the position of the sun combined with the regular phase difference between the *S2* and *M2* tides causes satellite sampling to alias tidal variations: different tidal signals become indistinguishable, or aliases of one another (Doxaran et al., 2009; Valente and Da Silva, 2009; Van der Wal et al., 2010). Secondly, the optical signal measured by the satellite sensor is influenced most by the top layer (El Serafy et al., 2011). Concentrations near the bed – often a short-term SPM source – can be higher when the water column is not fully mixed (Pietrzak et al., 2011). Finally, bias may arise because of selective sampling by the satellite sensor for cloud-free, calm conditions, whereas cloud cover in temperate regions is usually higher during the passage of fronts and the winter storms that resuspend SPM (Eleveld, 2012). Seasonality in cloudiness and rain likely also correlates with river discharge (Bouwer et al., 2006). Thus, resulting temporal snapshots of estuarine dynamics can also be expected to give biased responses to meteorological forcing.

In this paper, we examine the relation of SPM with tidal and meteorological drivers using MERIS data of the Westerschelde (Western Scheldt), a shallow macrotidal estuary in the southwest of the Netherlands (Fig. 1), which has also been modelled with a 3D mud transport model by Van Kessel et al. (2011). We specifically address issues relevant for the further use of estuarine SPM patterns from sun-synchronous satellite sensors, such as: (1) which co-occurring phases or tidal processes are sampled or missed, and how does this affect satellite SPM concentrations, and (2) what is the bias in the SPM signal caused by sampling under clear sky conditions?

For these purposes, we derived surface SPM maps, and investigated the spatial variation in SPM from satellite images and in situ data. Tidal variability is regularly cyclic and can be well-predicted. Meteorological variability is much less regular, but follows a seasonal cycle. We assessed the influence of tides, wind and river discharge in satellite SPM, by grouping the data collected under similar astronomical tidal or meteorological conditions. The impact of gradients in specific absorption and scattering characteristics was ascertained, providing an outlook for new algorithms that can handle such differences in absorption and scattering characteristics in the retrieval (Tilstone et al., 2012; Brando et al., 2012; Werdell et al., 2013). Finally, we used simulations from the mud transport model to support interpretation and quantify the biases in the satellite SPM signal due to tidal aliasing and due to cloud cover, respectively.

2. System description

For a range of estuaries worldwide, the Westerschelde has representative hydrodynamics, as its tidal amplitude (tidal prism of about 2×10^9 m^3) and friction characteristics approach average values (Toffolon et al., 2006). It is a typical tide-dominated coastal plain estuary which experiences a semi-diurnal tide; the mean tidal range increases from 3.8 m near the mouth to 5.0 m near the Dutch-Belgian border. Tidal discharge at the mouth is on average 50×10^3 m^3 s^{-1} (Chen et al., 2005), whereas river discharge is relatively low, and varies from ca 20 m^3 s^{-1} in summer to 180 m^3 s^{-1} in winter (Baeyens et al., 1998). The Westerschelde is quite well-mixed up to ca 40 km from the mouth, and partially mixed beyond this zone (Baeyens, 1998). Upstream of the lower outer Westerschelde estuary, a brackish inner upper estuary forms part of the River Zeeschelde (Fig. 1). The main estuarine turbidity maximum (ETM) is situated in this Zeeschelde, 60 to 100 km from the mouth of the Westerschelde, depending on tidal conditions and river discharge (Fettweis et al., 1998). A major coastal turbidity maximum (TM) is found along the North Sea shore south of the Westerschelde near Zeebrugge (Fig. 1) where Channel waters and (Rhine, Meuse, Westerschelde) river waters meet (Lacroix et al., 2004; Baeye et al., 2011).

PLEASE INSERT FIG. 1

3. Materials and methods

3.1. SPM from remote sensing

Reflectance measurements from the top of the water column were obtained from remote sensing using time-series of MERIS data. MERIS is a multispectral sensor on board ESA's sun-synchronous (polar orbiting) Envisat satellite, and captures images in several narrow optical and near-infrared bands (Table 1) with a ground resolution of ca 300 m (Full Resolution). From the EOLI-SA image archive, we selected all images from the period 2006-2008 that contained little or no cloud; these are 84 images, acquired between 9:58 and 10:58 UTC. The obtained Level 2 (L2) data were already processed up to water-leaving reflectance with standard ESA atmospheric correction, MEGS 7.4/IPF 5.05 (Moore and Aiken, 2000).

These remote measurements of electromagnetic radiation can be used for retrieving concentrations of optically active substances such as SPM, once their absorption and scattering properties are known:

$$\rho_{rs} = f(a, b, \theta_s, \theta_v, \phi, \lambda) \tag{1}$$

Remote sensing reflectance (ρ_{rs}) is a function (f) of a the total absorption and b total scattering, θ_s the solar zenith angle , θ_v viewing zenith angle, and ϕ differential azimuth angles, and λ wavelength. Total a and b of natural waters can be decomposed into the optical properties of pure water and its constituents by (Hoogeboom et al., 1998; Vos et al., 2003; Hommersom et al., 2010):

$$a = a_w + a^*_{CHL} CHL + a^*_{SPM} SPM + a^*_{CDOM} g_{440} \tag{2}$$

$$b = b_w + \frac{b^*_{bSPM}}{B} SPM \tag{3}$$

Total absorption a is the sum of a_w the absorption by pure water, a^*_{CHL} the mass-specific absorption of pigments times CHL, chlorophyll-a concentration, a^*_{SPM} the mass-specific absorption of non-algal particle pigments times SPM concentration, and a^*_{CDOM} specific coloured dissolved matter absorption normalised at 440 nm times absorption of $CDOM$ at 440 nm. Similarly, total scattering b is the sum of scattering by water b_w and particles, b^*_{bSPM} is specific particle backscattering and B backscattering ratio. Remote sensing reflectance, and all inherent optical properties (IOPs, the a's and b's) and specific inherent optical properties (sIOPs the a^*s and b^*s) are wavelength (λ) dependent.

For these waters with several optically active components, empirical concentration retrieval algorithms introduce inaccuracies for many wavelengths in the optical range. Algorithms based on near-infrared bands might suffer from adjacency effects (Santer and Schmechtig, 2000). Although various suitable MERIS coastal water algorithms are available (Moore et al., 1999; Doerffer and Schiller, 2007; Schroeder et al., 2007), HYDROPT (Van der Woerd and Pasterkamp, 2008) allowed input of optical properties of the Westerschelde. HYDROPT comprises a forward model that generates remote sensing reflectance (ρ_{rs}) as a function of the IOPs absorption (a) and scattering (b), and solar and viewing angles and is based on radiative transfer modelling with Hydrolight (Mobley and Sundman, 2001).

HYDROPT was parameterized with mean sIOPs (i.e., absorption and scattering coefficients normalised to concentrations) taken from earlier cruises carried out in the Westerschelde (cruises Restwes1999 and Oroma2002) and adjacent North Sea (Belgica 2000) where radiance was measured in situ with a PR-650 field-spectroradiometer (Photo research, Chatsworth, CA, USA). Water samples were filtered to measure SPM concentrations; extraction in ethanol allowed determination of chlorophyll-a (and phaeopigments) concentrations. Spectra of absorption (a) and beam attenuation (c) were measured using a Philips PU8800 UV/VIS double-beam lab-spectrophotometer. The scattering coefficient (b) was estimated by subtraction of the absorption coefficients from the beam attenuation coefficient (Rijkeboer et al., 1998). We tested the quality of these IOPs by optical modelling and comparison with the concurrently collected spectra. The remaining 11 sIOP sets for the North Sea were averaged, and the 25 for the Westerschelde were averaged too. On average specific backscattering (b^*_{SPM}) and absorption (a^*_{SPM}) of SPM were higher in the Westerschelde, than in the adjacent North Sea, but sIOPs are variable in space and time (Astoreca et al., 2009; Astoreca et al., 2012; Tilstone et al., 2012).

The inverse model estimates the concentrations of the constituents from remote sensing reflectance at several optical wavelength intervals using Levenberg-Marquard optimization. The optical model enables retrieval of SPM concentrations between 0.1 and 200 g m^{-3}. For this, MERIS bands 2 to 7 and 9 (Table 1) were used. Band 1 was discarded due to its sensitivity to errors in atmospheric correction and band 8 was excluded because of a possible contribution of fluorescence to the reflectance signal (Van der Wal et al., 2010), although sensitivity tests showed that in- or exclusion of the latter band only had minor impact on SPM retrieval.This is in line with with Gillerson et al. (2007), who showed that in our case, fluorescence is indeed effectively undetectable in the reflectance NIR peak. HYDROPT uses the difference in observed reflectance in consecutive bands in its spectral matching. Therefore it is less prone to failure when used with poor-quality (e.g., negative) input water reflectance (Stumpf and Werdell, 2010; Eleveld, 2012).

All images were re-projected to the Dutch coordinate system (Rijksdriehoeksstelsel). Values of SPM were extracted from the images at the location of in situ stations and along the estuarine thalweg (Fig. 1). In this study, we used mainly SPM retrieved from Westerschelde sIOPs. Additional results from parameterisation with North Sea sIOPs were only used to study their effect on the retrieval of SPM along the thalweg.

PLEASE INSERT TABLE 1

3.2. In situ measurements of SPM

An independent dataset (NIOZ database) contains SPM measured in situ in the period 2006-2008 at the water surface at 13 stations in the lower estuary (Westerschelde) and upper estuary (Zeeschelde up to Antwerpen) (Fig. 1), with a frequency of ca 20 times per year (but not during storms). Most samplings were carried out in two days, the first day in the lower and middle estuary (from WS1 to WS7) and the second day in the upper estuary (WS8 to WS13), following an up-river ship trajectory. SPM was determined gravimetrically after filtration on pre-combusted (400 °C, 4 h) Whatman GF/F filters. The volume of filtered water depended on the concentration of suspended matter in the sample. The filters were rinsed three times with milli-Q water, and dried at 60 °C.

3.3. Comparison of remotely sensed SPM with in situ measurements of SPM

To compare two independent distributions of in situ and remotely sensed data, we follow a well-accepted model (Campbell, 1995) for capturing bio-optical variability at a variety of spatial and temporal scales (IOCCG, 2006; Eleveld et al., 2008). Geometric mean SPM concentrations, i.e., averages of log-transformed values (we used log to base 10) were calculated at the NIOZ stations for all in situ data, in situ data within the time window of image acquisition (between 09:58 and 10:58 UTC), as well as for available satellite images (Eleveld et al., 2008). The time window corresponds with the range of acquisition times for the satellite data and, despite the different dates, a maximum time-difference of only one hour between satellite and in situ sampling can occur, which will be important in accounting for tidal aliasing. However, only 104 out of 517 in situ SPM measurements remained, and stations W5-W9 were not sampled, when only data collected between 09:58 and 10:58 UTC were considered.

3.4. Tides, wind/wave conditions and river discharge

The Dutch water monitoring programme (MWTL database, Rijkswaterstaat, 2013) contains fixed tidal stations in the thalweg of the Westerschelde estuary, including stations Vlissingen (VLI, local water depth ca 19 m), Terneuzen (TER, depth ca 33 m), Hansweert (HAN, depth ca 17 m) and Schaar van Ouden Doel (SCH) (Fig. 1). For each station, the tidal phase associated with time of image acquisition was calculated. For the semi-diurnal phase, predicted tidal harmonics at Oostende (MUMM, 2012) were used to forecast time after High Water at station VLI (time difference of 55 min with Oostende), TER (74 min), HAN (111 min) and SCH (145 min). The spring-neap cycle of each of the satellite images, expressed as a factor ranging from 0 (neap tide) to 1 (spring tide), was calculated from the illuminated fraction of the moon (Van der Wal et al., 2010; United States Naval Observatory, 2013) and the age of the tide at VLI (spring tide occurs ca 2 days after new and full moons). Results were checked with observations of water height at the MWTL stations (Rijkswaterstaat, 2013). Hourly tidal surface current velocities at stations VLI, TER, HAN and SCH for spring and neap tide were obtained from the Dutch tidal currents atlas (Dienst der Hydrografie, 2002). Hence, satellite derived SPM concentrations at the four MWTL stations could be analysed as a function of tidal phases and associated current velocities.

Daily wind data were obtained from the meteorological station at Vlissingen (situated near VLI) (Royal Netherlands Meteorological Institute, 2013), and daily river discharge measurements of the Scheldt were obtained from station Schaar van Ouden Doel (SCH) (Rijkswaterstaat, 2013), all for 2006, 2007 and 2008.

3.5. SPM against environmental conditions

To assess longitudinal gradients, SPM derived from the satellite along the thalweg and in situ SPM at stations were averaged for four broad categories of tidal phases in the semi-diurnal tidal cycle, based on high water at station HAN, a representative mid-estuary station, and for four stages in the neap-spring cycle (Table 2). Such a combination of data collected at similar tidal stages stresses astronomical variability and suppresses (averages out) variability in meteorological drivers such as wind waves, and discharge. To capture these bulk meteorological conditions, geometric mean SPM was also compared among the meteorological seasons (Table 2). Also, the effect of optical properties was studied by comparing geometric mean SPM from both Westerschelde and North Sea parameterisations along the thalweg.

Finally, composites of the satellite-derived log-transformed SPM maps were created to better reveal spatial patterns in SPM as a function of the semi-diurnal tidal phase, fortnightly tidal phase, and seasons (Table 2), respectively. Every pixel giving a valid SPM value for water was used, and because the original images contained little or no cloud (Section 3.1), pixel-based averages were generally based on the total number of images in each class. Note that mean of intertidal shallow areas is based on a limited number of samples.

PLEASE INSERT TABLE 2

3.6. SPM from modelling

To help with the interpretation, we used output from an independent 3D mud transport model for the Westerschelde for 2006. The model is based on an advection–diffusion solver implemented in DELFT3D-WAQ, and uses output at 30 min intervals for 3D velocity fields and water levels from a decoupled hydrodynamic model set up in TRIWAQ/SIMONA (Van Kessel et al., 2011).

The model was also used to test for biases in sampling. We considered half hourly model output at MWTL stations for all conditions to be an unbiased reference. Filtered output for zero octant cloud cover at Vlissingen (Royal Netherlands Meteorological Institute, 2013) was considered a proxy for clear skies, filtered output from 10:00 – 11:00 UTC a proxy for the tidally aliased conditions at overpass, and zero cloud cover at overpass a proxy for satellite observations.

4. Results and interpretation

4.1. Comparison of SPM from remote sensing and in situ measurements

At the NIOZ stations, geometric mean satellite SPM correlated significantly with independent geometric mean in situ SPM ($r=0.89$, $n=13$, $p<<0.01$, $y= 1.48x - 0.78$ for the arbitrary choice of log in situ SPM as x and log remote sensing SPM as y, Fig. 2). Both increased with distance from the mouth. Satellite SPM is underestimated at the most seaward stations (notably W1 and W2). We used a lognormal distribution because SPM is positively skewed and has a lognormal distribution, but the linear inter-comparison is also highly significant ($r=0.82$, $n=13$, $p<<0.01$, $y= 1.03x + 1.23$), and all results are within the 100% error bounds.

When tidal aliasing is taken into account by using only in situ data collected between 9:58 and 10:58 UTC, the Pearson correlation remains significant ($r=0.87$, $n=7$, $p=0.01$, $y= 1.21x - 0.49$), although fewer stations with in situ data remain. Underestimation of SPM from remote sensing at the mouth and overestimation up-river will be examined further in section 4.4.

PLEASE INSERT FIG. 2

4.2. Satellite SPM at specific tidal phases and associated current velocities

To quantify astronomic impact, satellite derived SPM concentrations extracted at four MWTL stations for all 84 images are shown as a function of tidal components (Fig. 3a-d). Highest SPM concentrations (largest dots) occur at 6 to 4 h before HW (-6 to -4 h), -1 h, and from 4.5 to 6 h after HW (+4.5 to +6 h). All individual phases of the semi-diurnal tide (which is on the x-axis), and neap-spring phases (on the y-axis) were sampled, but the combinations of semi-diurnal and neap-spring tides are fixed at overpass. The overall sinusoidal patterns in Fig. 3a-d demonstrate the co-occurrence of semi-diurnal and neap-spring phases, or tidal aliasing at the satellite's sun-synchronous overpasses.

For all stations, surface tidal current velocities are highest at -1 h, and +4 to +6 h, and lowest at slack -5 h and +1 h (Fig. 3e-h). Station VLI – with high current velocities before HW – is flood-dominant, whereas SCH has slightly higher ebb-currents. The exchange of larger water volumes causes higher current velocities at spring than at neap; tidal aliasing controls which currents within these envelopes can actually be sampled (Fig. 3e-h).

Hence, high SPM in Fig. 3a-d may be explained by sediment transport from tidal flats during shallow water conditions (-6 to -4 h), high tidal current velocities and mixing (-1 h), or a combination of the two (+4.5 to +6 h). The results also imply that tidal stage and currents that are favourable for high SPM are overrepresented in the satellite observations. After all, combinations of LW and spring (which implies a small distance to the sediment bed and strong currents), or HW at weak neap currents are sampled by the satellite.

4.3. Modelled SPM and hydrodynamics

Model results provide further insight into the mechanisms causing high SPM concentrations (Fig. 4). Two concentration peaks occur per tide: one just before high water and one at low water. The modelled SPM peak at low water is highest. This is because of a decreasing concentration gradient from east (Antwerpen) to west (VLI), which implies transport of waters with a relatively high SPM at ebb. In addition, mud is resuspended and transported with the remaining water flowing of the tidal flats. This is in line with the relatively high satellite SPM values before LW (Fig. 3a-d). Fig. 4 also illustrates that modelled SPM concentration peaks at the surface lag behind modelled peaks in ebb and flood currents and shear stress at the bottom, because it takes time for SPM to mix up from deeper areas.

PLEASE INSERT FIGS 3 AND 4

4.4. Longitudinal gradients in SPM and environmental conditions

Geometric mean satellite derived SPM increases along the thalweg from Vlissingen to Antwerpen (Fig. 2 and 5). Further up-river (> 85 km from VLI), the river becomes too narrow for retrieval of concentrations from MERIS FR data. Satellite derived SPM is highest during shallow water conditions at low water and during ebb tide, followed by flood, and lowest at high water (Fig. 5a). Likewise, SPM is highest when huge water volumes are exchanged, at mean to spring and spring, followed by neap to mean, and lowest for neap when currents are weak (Fig. 5b). The same class sequencing was found for similarly classified in situ SPM (Fig. 5a and b). Note that satellite-derived concentrations at LW and HW (Fig. 5a), resemble those at spring and neap (Fig. 5b) respectively, due to tidal aliasing. Tidally classified SPM values range between 1.58 times larger and smaller than geometric mean, (this is $10^{0.2}$ in Fig. 5a, b), and this factor does not change with distance.

Seasonal averages show high SPM in the inner estuary in spring (55- 85 km from VLI, Fig. 5c). Probably, the estuarine turbidity maximum (ETM) is captured as it moves seaward and appears in our transect after high river discharge (Rijkswaterstaat, 2013; Section 2). High concentrations in the outer estuary (< 40 km from VLI) result from resuspension by winter storms with a long fetch (Fig. 5c). Hence, the seasonal approach likely captures residence and net settling times. Note that daily wind velocity is, on average, slightly higher during in situ campaigns (5.5 m s^{-1}) than at image acquisition (4.8 m s^{-1}) (t-test, $t=2.01$, $df=125$, $p<0.05$). This may partly explain why satellite SPM is lower than in situ SPM at the mouth (<12 km from VLI) (Fig. 5d; Fig. 2).

In addition, comparison of geometric mean SPM derived with sIOPs of North Sea and Westerschelde water (Fig. 5d) confirms that at the mouth, SPM concentrations are higher and better predicted when the retrieval algorithm was parameterised with optical properties of North Sea water. In contrast, from ca 35 km up-estuary, predictions based on North Sea sIOPs are lower than those from Westerschelde sIOPs, and often lower than in situ SPM.

PLEASE INSERT FIG. 5

4.5. SPM composites

SPM composites quantify near-surface spatial heterogeneity at estuarine scale for different tidal stages. At low water (Fig. 6a), the geometric mean composite displays high SPM (> 30 mg l^{-1}), because of the shallow water column. The impact of currents is secondary, as this composite comprises a mixture of surface water flows: incoming North Sea waters (between -6 and -4.5 h before HW HAN) with weak currents at LW slack (-5 h), and stronger outgoing currents of Westerschelde waters (between +4.5 and +6 h, see Table 2, Fig. 3g). During flood (Fig. 6b), the channels are accentuated, because incoming North Sea waters are generally lower in SPM than ambient concentrations in the Westerschelde estuary proper. Remember also that the composites were based on SPM concentrations derived with Westerschelde sIOPs that underestimate North Sea SPM (Fig. 5d). The HW composite (Fig. 6c) also features low surface SPM concentrations (< 30 mg l^{-1}), that stretch from the mouth to ca 45 km up the estuary. This composite quantifies the dual response of SPM to strong, landward directed surface currents (at -1 h +HW HAN), and weak seaward currents (at HW slack, +1 h +HW HAN, Fig.3). During ebb tide (Fig. 6d), seaward directed surface currents entrain and advect high SPM concentrations (> 30 mg l^{-1}), which obscures the distinction between channels and flats in the composite. Composites of the fortnightly cycle confirm concentration ranges from the thalweg (Supplementary Fig. S1 versus Fig. 5b); due to tidal aliasing, patterns at neap strongly resemble the associated HW composite, while those at spring tide resemble the LW composite.

In all tidal composites except HW and (coinciding) neap, two turbidity maxima can be discerned, one ETM at the lower reaches of the Zeeschelde (River), and one TM near Zeebrugge (in a shallow, 2 to 5 m deep part of the North Sea). Surface concentrations in these turbidity maxima do differ per composite; hence they are influenced by tide. Their location suggests influence of river discharge and wind (fetch), respectively. Indeed, the winter and spring season composites (Fig. 7) show high SPM in the Zeeschelde (river) from SCH to Antwerpen. Peak discharge (> 200 m s^{-1} at SCH) occurs in the winter months and in March when more cloud-free satellite data were available. The seasonal composites also show high SPM concentrations (> 75 g m^{-3}) near Zeebrugge (North Sea) in winter when wind speeds greater than 10 m s^{-1} occurs most frequently (Royal Netherlands Meteorological Institute, 2013).

Fig. 6 and 7 present surface SPM values within similar ranges, which suggests that within the estuary proper, the impact of meteorological drivers is similar to that of tidal drivers. Winter notably presented higher values offshore, which are likely caused by wave resuspension.

PLEASE INSERT FIGS 6 AND 7

4.6. Quantification of biases in the satellite SPM signal

A statistical analysis on daily observations of cloud cover and wind at Vlissingen (1 Jan. 2006 – 31 Dec. 2008) confirmed that mean daily wind velocity is significantly higher on days with (1-8 Octants) than on days without cloud cover (0 Octants) (one-way ANOVA with posthoc HSD test for unequal sample sizes, $F_{1,1089}$=33.928, n=1091, p<0.0001). Wind velocity was on average 6.3 m s^{-1} on cloudy days versus 4.5 m s^{-1} on clear days. In addition, mean daily wind velocity increased significantly with Octants cloud cover (linear regression, R^2=0.11, $F_{1,1089}$=132.853, n=1091, p<0.0001). We used the independent 3D mud transport model for the Westerschelde for 2006 to quantify this and other effects of biased sampling on SPM. Compared with the average of all half-hourly SPM model output for 2006 (i.e. the unbiased SPM reference), average modelled SPM for clear sky conditions only was lower (with a relative error of between -7.86 and -2.03 % for geometric mean) throughout the estuary and particularly at the mouth (Table 3), indicating that fair weather sampling underestimates the detected SPM concentration.

We observed that polar-orbiting satellites sample all individual stages of the main (semi-diurnal and fortnightly) harmonic components, but not all combinations of the two due to tidal aliasing (Fig. 3), and observed that this causes a bias: tidal stage and currents that are favourable for high SPM, combinations of LW and spring or HW at weak neap currents are overrepresented in the satellite observations (Section 4.2). Indeed, selected model output between 10:00 – 11:00 UTC (i.e., tidally aliased conditions at overpass), also gave slightly higher SPM concentrations than the reference (relative error 0.04 to 2.91 %). Thus, we quantified the tidal bias inherent to an optically sound set-up; having a satellite in sun-synchronous orbit.

A combination of the two criteria, which likely represents actual image acquisition conditions, resulted in an underestimation of the SPM concentrations relative to unbiased conditions (relative error -8.07 to -0.38 %). Again, underestimation was largest at the mouth of the estuary, and smallest in the upper estuary. Hence, the underestimation due to clear weather conditions is stronger than the overestimation due to tidal aliasing in the Westerschelde, particularly for the wind exposed and flood-dominant station VLI (Table 3).

PLEASE INSERT TABLE 3

5. Discussion and conclusion

5.1. Exposed mechanisms

Ocean colour remote sensing data captured SPM concentrations for the full extent of the outer estuary and part of the inner estuary, and is the only observation technique that can generate empirical evidence for regularities in SPM concentrations from bulk tidal, and bulk meteorological drivers with such coverage (Shi et al., 2011; Eleveld, 2012). Our tidal composites gave a 2D overview of tidal advection of North Sea and estuarine surface waters (Fig. 6b and d), and showed the impact of (vertical) mixing in the spring-neap composites (Supplementary Fig. S1). The seasonal composites gave high concentrations in the upper estuary from 40 km (HAN) landward in spring, and from 40 km seaward in winter.

The two turbidity maxima in these two regions, one in the upper estuary and one offshore express the resultant of coupled current, stratification and turbulence interactions at the surface (Burchard et al., 2008; Pietrzak et al., 2011). They were only visible during favourable tidal conditions, and high discharge or wind, respectively. Similarly to Doxaran et al. (2009) for the Gironde, we find high concentrations at spring tide, because the exchange of large water volumes inevitably leads to both more horizontal advection and better vertical mixing to surface, and in winter and spring when peak discharges occur (Fig. 7). For the outer estuary, the link with instantaneous discharge is weak, probably because Westerschelde river runoff is low compared with the volume of the estuary, which results in a stable – both in time and space – and very gradual salinity gradient, and a residence time of about 75 days for the entire estuary (Muylaert and Sabbe, 1999). Visibility of the TM near Zeebrugge over the Flemish banks requires tidal or wind mixing in this area of the Rhine region of fresh water influence (ROFI, Simpson et al., 1993). Otherwise, when stratified, surface SPM concentrations are low despite high sub-surface concentrations near Zeebrugge (Eleveld et al., 2008; Pietrzak et al., 2011).

The large fetch enables wind-waves to resuspend sediments near Zeebrugge and most of the outer estuary (Van der Wal et al., 2008; Callaghan et al., 2010; Eleveld, 2012), and thus it is revealed as high surface SPM in winter, and hardly visible during the calm summer season (Fig. 7c). Our results indicate that wave energy becomes negligible compared with tidal energy upstream of 40 km (Fig. 5c) where local wind-waves are fetch-limited. Some stratification and flocculation may occur, as 40 – 60 km is also the maximum distance for salinity intrusion during high river runoff (Verlaan et al., 1998; Chen et al., 2005). Observed controls for surface SPM concentrations from the satellite dataset are: (1) horizontal and vertical distance to shallow source areas, observed as tidal stages (Fig. 3a-d, and Fig. 6 and 7, and Supplementary material S1), (2) high tidal current velocity (compare Fig. 3a-d and 3e-h) and wind (Fig. 5c and 7), and (3) advection of North Sea surface waters during flood and estuarine surface waters during ebb tide (Fig. 6d and 6b, respectively).

5.2. Universality of biases

For the Westerschelde estuary, SPM from optical observations at satellite overpass tends to be low, because cloud-free images are usually associated with calm conditions. On the other hand, high SPM results from combinations of LW and spring (*viz*. small distance to the bed and extreme flow conditions). Hence we found increased SPM, even though aliasing also implies that the effect of antagonistic mixing and stratification processes is sampled: Simpson et al. (1990) showed that the water column is well-mixed during spring tide, flood or high water, whereas it is periodically stratified at neap, ebb or low water. Our independent model simulation demonstrated that the underestimation due to fair weather was stronger than the overestimation due to tidal aliasing, for the wind-exposed and flood-dominant station at the mouth (a -8% net relative error results). Such a bias, which has not been quantified before, needs to be considered in the interpretation of water quality products from remote sensing, for example when causal links with climate indices and teleconnections are sought (Fettweis et al., 2012).

How generic are these biases? As the tidal amplitude and phase depend on the earth-moon-sun geometry, as well as on distance from amphidromic points and bottom friction, there is always a relationship between tidal constituents, e.g., semi-diurnal phase and fortnightly phase, or diurnal and tropically driven neap-spring cycles (Kvale, 2006) for a specific time. This association varies in space: it differs both among and within estuaries. Some coupling of harmonics is generic, but implications for SPM are location specific, because each coastal stretch or estuary has different bottom friction/topography and distance from amphidromic points. Some estuaries are also less tide dominated (Dalrymple et al., 1992; Toffolon et al., 2006), causing the numerical impact of the astronomical bias on SPM to decrease. We found location-dependent impact of the selective sampling for cloud-free conditions within the estuary, as low SPM at the wind wave dominated mouth (Table 3). An underestimation of SPM due to a fair weather sampling bias is likely generic in regions where weather changes are largely associated with the passage of fronts, but the biases may differ for other atmospheric and ocean circulation conditions. To elucidate this, the global latitudinal and seasonal effects of local cloud cover on the proportion of missing satellite observations (Cole et al., 2012) should be linked with global circulation patterns.

5.3. Methodological implications

Relatively small case-2 waters pose particular challenges for robust retrieval of satellite SPM. The HYDROPT processing has been performed on pixels that had been classified as water, not land or cloud in the standard MERIS L2 processing (Santer et al., 1997; Moore and Aiken, 2000). Fig. 6 and 7 clearly illustrate that the satellite captures the main spatio-temporal variability for the overall estuary. This is also true for individual images, and is also confirmed by model results (see also Fig. 10 of Van der Wal et al., 2010). Most of the analyses (Fig. 2-5) were performed (at stations) along the deep thalweg (Fig. 1). At some locations where the thalweg approaches the coastline (W6, W12 and W13, see Fig. 1) we may occasionally suffer from inaccuracies for the first pixel (geometric inaccuracies which could cause a shift of one pixel, and perhaps mixels or adjacency effects, see Fig. 3 of El Serafy et al., 2011). Most stations though, are several pixels away from the coastline. Emerged tidal flats are classified as land, and the sensor does not measure bottom reflectance for submerged flats in these extremely turbid waters (Hommersom et al., 2010). These are all issues that are under study in the MERIS reprocessing.

The general performance of HYDROPT for these waters could also be assessed by inspecting the additionally retrieved CHL and CDOM concentrations (Van der Woerd and Pasterkamp, 2008; Tilstone et al., 2012). For the Westerschelde, the number of valid retrievals for CHL and CDOM is somewhat less than for SPM, but performance is good. Both in situ (NIOZ database) and remotely sensed (HYDROPT) CHL are generally 3-10 μg/l. In situ and remote sensing CHL data both capture similar timing and high concentrations of the spring bloom, which was also perceived just offshore for 2003 by Van der Woerd et al. (2011). We do not have sufficient in situ data to check the CDOM retrieval, but the retrieved g_{440} values range from 0.2 m^{-1} (at VLI) to >2 m^{-1} (85 km from VLI) as we would expect for the Westerschelde (Astoreca et al., 2009).

Results from re-parameterisation with North Sea sIOPs (Fig. 5d) showed the quantitative implications that different optical properties have on the retrieval of SPM gradients in the Westerschelde estuary. We suggest to classify sIOPs by tide, and by water type (based on CTD measurements), before applying adaptive inverse modelling (Brando et al., 2012; Tilstone et al., 2012) to improve physical understanding of the retrieval.

Our results also demonstrate the benefits of the classification method used to separate tidal from meteorological dynamics. Mechanisms likely causing the main observed differences between the classes could be revealed (sections 4.5 and 5.1) because the geometric means carry tidal and seasonal information, respectively. Apparently, these broad groups contain sufficient images per class, and allow for the time that it takes for semi-diurnal tides to propagate through the estuary (cf. Section 3.4) and lags between surface flow, bottom shear and SPM expression at surface (Section 4.3, Fig. 4). However, the fast flood and slow ebb currents ended up in the same class (i.e., HW, Section 4.5). An alternative method for larger datasets could be to carefully expand the number of classes, investigate tidal classes for specific seasons to capture seasonal changes in sIOPs, or to subject the SPM maps to a harmonic analysis (Pietrzak et al., 2011). Although we typically had a limited number of cloud-free winter images (Table2; Pietrzak et al., 2011), the distribution of the images over the tidal phases is quite similar so one can safely compare between phases (Supplementary Material S2).

MERIS on the ENVISAT platform, the Moderate Resolution Imaging Spectroradiometer (MODIS) on the Aqua and Terra satellites, and the Ocean Land Colour Instrument (OLCI) onboard the planned Sentinel 3 mission are all on sun-synchronous low earth orbit (LEO) platforms. Derived SPM maps are being interpreted by many scientists (Knaeps et al., 2012; Vantrepotte et al., 2013), and if these are used in (spatio-)temporal interpolations (Nechad et al., 2011) the previously mentioned biases (Section 5.2) have to be taken into account, e.g. by using a process-based model to interpolate between missing values (El Serafy et al., 2011). Alternatively, instruments on geostationary satellites, such as the Spinning Enhanced Visible and Infrared Imager (SEVIRI onboard METEOSAT, Neukermans et al., 2009) or the high resolution Geostationary Ocean Colour Imager (GOCI onboard COMS, Choi et al., 2012) can now provide images every 15 min or hour during daytime (adequate solar zenith angles), respectively. These satellites rotate around the same axis as the earth and at exactly the same speed, keeping them pointed permanently at the same point on earth (IOCCG, 2012). Their very high temporal coverage enables to better resolve the independent semi-diurnal and neap-spring dynamics in SPM.

5.4. Conclusion: tidal and seasonal biases and effects

In this paper, we elucidate the problems and we demonstrate technical solutions that aim to advance the use of remotely sensed data for investigating dynamic coastal environments. We demonstrated that astronomical, meteorological and biogeochemical (water constituents) biases in the extremely variable concentrations of water quality parameters from sun-synchronous satellite remote sensing can be substantial, and also vary both in time and space, thus posing a challenge for quantifying estuarine SPM from (sun-synchronous) satellite remote sensing. Based on meaningful composites that link several individual drivers to SPM response and average out variability by other drivers, we conclude that tide, and locally fresh water discharge and wind explain most of the variation in observed surface SPM concentrations for the Westerschelde, and that the extent and magnitude of astronomic and seasonal effects on the variation of SPM is similar in the estuary proper (Fig. 6 and 7). With surface SPM and its controls, we capture many of the environmental drivers for primary production in these light limited ecosystems. Hence, we can safely state that the emergent SPM signal in the satellite data provides synoptic information that will further our understanding of the dynamics of estuarine systems.

Acknowledgements

This work was partly carried out within the framework of LTV (Long Term Vision Westerschelde) for which we also thank Luca van Duren (Deltares) and Joris Vanlede (WL Borgerhout). The European Space Agency provided MERIS-FR data within ESA Cat-1 project 4453. We acknowledge Machteld Rijkeboer, Steef Peters and Reinold Pasterkamp (IVM), in collaboration with MUMM and Rijkswaterstaat MD, for databases with historic sIOPs, and Reinold Pasterkamp for the HYDROPT Software library. Rijkswaterstaat is acknowledged for the MWTL in situ data, and NIOZ Yerseke (former NIOO-CEME) for the NIOZ in situ data. We thank Peter Verburg and Alison Gilbert (VU-IVM) for comments on the manuscript, and Annette Wielemaker-van den Dool (NIOZ Yerseke) for help with KML.

Appendix A. Supplementary data

Supplementary data associated with this article can be found in the online version, at http://dx.doi.org/10.101 6/j.rse.2 013.12.019. These data include cross-tabulations (Table S1), neap-spring composites (Fig. S1) and a KMZ file of the flood composite (Fig 6b) on a Google Earth background.

References

Astoreca, R., Doxaran, D., Ruddick, K., Rousseau, V., & Lancelot, C. (2012). Influence of suspended particle concentration, composition and size on the variability of inherent optical properties of the Southern North Sea. *Continental Shelf Research*, *35*, 117-128.

Astoreca, R., Rousseau, V., & Lancelot, C. (2009). Coloured dissolved organic matter (CDOM) in Southern North Sea waters: Optical characterization and possible origin. *Estuarine, Coastal and Shelf Science*, *85*, 633-640.

Baeye, M., Fettweis, M, Voulgaris, G., & Van Lancker, V. (2011). Sediment mobility in response to tidal and wind-driven flows along the Belgian inner shelf, southern North Sea. *Ocean Dynamics*, *61*, 611-622.

Baeyens, W., van Eck, B., Lambert, C., Wollast, R., & Goeyens, K. (1998). General description of the Scheldt estuary. *Hydrobiologia*, *366*, 1-14.

Bale, A. J., Tocher, M. D., Weaver, R., Hudson, S. J., & Aiken, J. (1994). Laboratory measurements of spectral properties of estuarine suspended particles. *Netherlands Journal of Aquatic Ecology*, *28*, 237-244.

Blondeau-Patissier,D., Brando, V. E., Oubelkheir, K., Dekker, A. G., Clementson, L. A. & Daniel, P. (2009). Bio-optical variability of the absorption and scattering properties of the Queensland inshore and reef waters, Australia. *Journal of Geophysical Research-Oceans*, *114*, C05003, doi:10.1029/2008JC005039

Bouwer, L. M., Vermaat, J. E. & Aerts, C. J. H. J. (2006). Winter atmospheric circulation and river discharge in northwest Europe, *Geophysical Research Letters*, *33*, L06403, doi:10.1029/2005GL025548.

Bowers, D. G., Braithwaite, K. M., Nimmo-Smith, W. A. M., & Graham, G. W. (2009). Light scattering by particles suspended in the sea: The role of particle size and density *Continental Shelf Research*, *29*, 1748-1755.

Brando, V., Dekker, A., Park, Y., & Schroeder, T. (2012). Adaptive semianalytical inversion of ocean color radiometry in optically complex waters. *Applied Optics*, *51*, 2808-2833.

Burchard, H., Flöser, G., Staneva, J. V., Badewien, T. H., & Riethmüller, R. (2008). Impact of density gradients on net sediment transport into the Wadden Sea. *Journal of Physical Oceanography*, *38*, 566-587.

Callaghan, D. P., Bouma, T. J., Klaassen, P., van der Wal, D., Stive, M. J. F., & Herman, P. M. J. (2010). Hydrodynamic forcing on saltmarsh-development: distinguishing the relative importance of waves and tidal flows. *Estuarine, Coastal and Shelf Science*, *89*, 73-88.

Campbell, J. W. (1995). The lognormal distribution as a model for bio-optical variability in the sea. *Journal of Geophysical Research*, *100*(C7), 13237–13254. doi:10.1029/95JC00458.

Chen, M. S., Wartel, S., van Eck, B., & van Maldegem, D. (2005). Suspended matter in the Scheldt estuary. *Hydrobiologia*, *540*, 79-104.

Choi, J.-K., Park, Y. J. Ahn, J. H., Lim, H. S., Eom, J., & Ryu, J.-H. (2012). GOCI, the world's first geostationary ocean color observation satellite, for the monitoring of temporal variability in coastal water turbidity, *Journal of Geophysical Research-Oceans*, *117*, C09004, doi:10.1029/2012JC008046.

Cloern, J. E. (1996). Phytoplankton bloom dynamics in coastal ecosystems: A review with some general lessons from sustained investigation of San Francisco Bay, California. *Reviews of Geophysics*, *34*, 127-168.

Cole, H., Henson, S., Martin, A., & Yool A. (2012). Mind the gap: The impact of missing data on the calculation of phytoplankton phenology metrics *Journal of Geophysical Research-Oceans*, *117,* C08030, doi:10.1029/2012JC008249.

Costanza, R., d'Arge, R., de Groot, R., Farber, S., Grasso, M., Hannon, B., Limburg, K., Naeem, S., O'Neill, R. V., Paruelo, J., Raskin, R. G., Sutton, P., & van den Belt, M. (1997). The Value of the World's Ecosystem Services and Natural Capital. *Nature*, *38*, 253-260.

Dalrymple, R. W., Zaitlin, B. A., & Boyd, R. (1992). Estuarine facies models: conceptual basis and stratigraphic implications. *Journal of Sedimentary Petrology*, *62*, 1130-1146.

Dienst der Hydrografie (2002). *Waterstanden, stromen, langs de Nederlandse kust en aangrenzend gebied.* (Tidal heights. Currents. Coastal waters of the Netherlands and adjacent areas.) HP33. Den Haag: Koninklijke Marine – Dienst der Hydrografie.

Doerffer, R., & Schiller, H. (2007). The MERIS case 2 water algorithm. *International Journal of Remote Sensing*, *28*, 517-535.

Doxaran, D., Froidefond, J.-M., Castaing, P., & Babin, M. (2009). Dynamics of the turbidity maximum zone in a macrotidal estuary (the Gironde, France): observations from field and MODIS satellite data. *Estuarine, Coastal and Shelf Science*, *81*, 321-322.

D'Sa, E. J., Miller, R. L., & McKee, B. A. (2007). Suspended particulate matter dynamics in coastal waters from ocean color: Application to the northern Gulf of Mexico. *Geophysical Research Letters*, *34*, L23611, doi:10.1029/2007GL031192.

Dyer, K. R. (1989). Sediment processes in estuaries: Future research requirements. *Journal of Geophysical Research-Oceans*, *94*(C10), 14327-14339.

Eleveld, M. A. (2012). Wind-induced resuspension in a shallow lake from Medium Resolution Imaging Spectrometer (MERIS) full-resolution reflectances. *Water Resources Research*, *48*, W04508, doi:10.1029/2011WR011121

Eleveld, M. A., Pasterkamp, R., van der Woerd, H. J., & Pietrzak, J. D. (2008). Remotely sensed seasonality in the spatial distribution of sea-surface suspended particulate matter in the southern North Sea. *Estuarine, Coastal and Shelf Science*, *80*, 103-113.

El Serafy, G. Y., Eleveld M. A., Blaas, M., van Kessel, T., Gaytan Aguilar, S., & van der Woerd, H. J. (2011). Improving the description of the suspended particulate matter concentrations in the southern North Sea through assimilating remotely sensed data. *Ocean Science Journal*, *46*, 179-204.

Fettweis, M., Sas, M., & Monbaliu, J. (1998). Seasonal, neap-spring and tidal variation of cohesive sediment concentration in the Scheldt estuary, Belgium. *Estuarine, Coastal and Shelf Science*, *47*, 21-36.

Fettweis, M., Monbaliu, J., Baeye, M., Nechad, B. & Van den Eynde, D. (2012). Weather and climate induced spatial variability of surface suspended particulate matter concentration in the North Sea and the English Channel. *Methods in Oceanography*, *3-4*, 25-39.

Forget, P., Ouillon, S., Lahet, F., & Broche, P. (1999). Inversion of reflectance spectra of nonchlorophyllous turbid coastal waters. *Remote Sensing of Environment*, *68*, 264-272.

Gallegos, C. L., Jordan, T. E., Hines, A. H., & Weller, D. E. (2005). Temporal variability of optical properties in a shallow, eutrophic estuary: Seasonal and interannual variability. *Estuarine, Coastal and Shelf Science*, *64*, 156-170.

Gattuso, J.-P., Frankignoulle, M., & Wollast, R. (1998). Carbon and carbonate metabolism in coastal aquatic ecosystems. *Annual Review of Ecology and Systematics*, *29*, 405–34.

Gilerson, A., Zhou, J., Hlaing, S., Ioannou, I., Schalles, J., Gross, B., Moshary, F., & Ahmed, S. (2007). Fluorescence component in the reflectance spectra from coastal waters. Dependence on water composition. *Optics Express*, *15*, 15702-15721.

Heip, C.H.R., Goosen, N. K., Herman, P. M. J., Kromkamp. J., Middelburg, J. J., & Soetaert, K. (1995). Production and consumption of biological particles in temperate tidal estuaries. *Oceanography and Marine Biology: an Annual Review*, *33*, 1-149.

Hommersom, A., Peters, S., van der Woerd, H. J., Eleveld, M. A., & de Boer, J. (2010). Chi-square spectral fitting for concentration retrieval, automatic local calibration, quality control, and water type detection. *Canadian Journal of Remote Sensing*, *36*, 650-670.

Hoogenboom, H. J., Dekker, A. G., & de Haan, J. F. (1998). Retrieval of chlorophyll and suspended matter from imaging spectrometry data by matrix inversion. *Canadian Journal of Remote Sensing*, *24*, 144–152.

IOCCG (2006). Remote Sensing of Inherent Optical Properties: Fundamentals, Tests of Algorithms, and Applications. In Z.-P. Lee (Ed.), *Reports of the International Ocean-Colour Coordinating Group*, Dartmouth, Canada, Vol. 5. http://www.ioccg.org/reports/report5.pdf Accessed Dec. 2013

IOCCG (2012). Ocean-Colour Observations from a Geostationary Orbit. In D. Antoine (Ed.), *Reports of the International Ocean-Colour Coordinating Group*, Dartmouth, Canada, *Vol. 12*. http://www.ioccg.org/reports/report12.pdf Accessed Dec. 2013

Knaeps, E., Dogliotti, A.-I., Raymaekers, D., Ruddick, K. & Sterckx, S. (2012). In situ evidence of non-zero reflectance in the OLCI 1020nm band for a turbid estuary. *Remote Sensing of Environment*, *120*, pp. 133–144.

Kvale, E. P. (2006). The origin of neap–spring tidal cycles. *Marine Geology*, *235*, 5–18.

Lacroix, G., Ruddick, K., Ozer, J., & Lancelot, C. (2004). Modelling the impact of the Scheldt and Rhine/Meuse plumes on the salinity distribution in Belgian waters (southern North Sea). *Journal of Sea Research*, *52*, 149-163.

Mélin, F., G. Zibordi, & J.-F. Berthon (2007). Assessment of satellite ocean color products at a coastal site. *Remote Sensing of Environment*, *110*, 192-215.

Meire, P., Ysebaert, T., Van Damme, S., Van den Bergh, E., Maris, T., & Struyf, E. (2005). The Scheldt estuary: a description of a changing ecosystem. *Hydrobiologia*, *540*, 1–11.

Middelburg, J. J., & Nieuwenhuize, J. (1998). Carbon and nitrogen stable isotopes in suspended matter and sediments from the Schelde Estuary. *Marine Chemistry*, *60*, 217–225.

Miller, R. L., & McKee, B. A. (2004). Using MODIS Terra 250 m imagery to map concentrations of total suspended matter in coastal waters. *Remote Sensing of Environment*, *93*, 259-266.

Mobley, C. D., & Sundman, L. K. (2001). *Hydrolight 4.2: Technical documentation*. Redmond: Sequoia Scientific. Available via http://www.sequoiasci.com/products/hl-radiative.cmsx. Accessed Dec. 2013.

Mobley, C. D., Stramski, D., Bissett, W. P., & Boss, E. (2004). Is the Case 1 - Case 2 classification still useful? *Oceanography*, *17,* 60-67.

Moore, G. F., Aiken, J., & Lavender, S. J. (1999). The atmospheric correction of water colour and the quantitative retrieval of suspended particulate matter in Case II waters: application to MERIS. *International Journal of Remote Sensing*, *20*, 1713-1733.

Moore, G. F., & Aiken, J. (2000), Case 2 (S) bright pixel atmospheric correction. *Algorithm Theor. Basis Doc. ATBD 2.6*, Issue 4, 1st rev., Plymouth Mar. Lab., Plymouth, UK. Available via https://earth.esa.int/instruments/meris/pdf/atbd_2_06.pdf Accessed Dec. 2013

MUMM (2012). *Harmonic tides predictor for Ostend*. Available via http://www.mumm.ac.be/EN/Models/Operational/Tides/predictor.php. Accessed Dec. 2013.

Muylaert, K., Sabbe, K. (1999). Spring phytoplankton assemblages in and around the maximum turbidity zone of the estuaries of the Elbe (Germany), the Schelde (Belgium/The Netherlands) and the Gironde (France). *Journal of Marine Systems*, *22*, 133–149.

Nechad, B., Alvera-Azcaràte, A., Ruddick, K., & Greenwood, N. (2011). Reconstruction of MODIS total suspended matter time series maps by DINEOF and validation with autonomous platform data. *Ocean Dynamics, 61*, 1205–1214.

Nechad, B., Ruddick, K.G., & Park, Y. (2010). Calibration and validation of a generic multisensor algorithm for mapping of Total Suspended Matter in turbid waters. *Remote Sensing of Environment*, *114*, 854-866.

Neukermans, G., Ruddick, K., Bernard, E., Ramon, D, Nechad, B., & Deschamps, P.-Y. (2009). Mapping total suspended matter from geostationary satellites: a feasibility study with SEVIRI in the Southern North Sea. *Optics Express*, *17*, 14029-14052.

Pietrzak, J. D., de Boer, G. J., & Eleveld, M. A. (2011). Mechanisms controlling the intra-annual mesoscale variability of SST and SPM in the southern North Sea. *Continental Shelf Research*, *31*, 594-610.

Rijkswaterstaat (2013). *Waterbase*. Available via http://live.waterbase.nl/ Accessed Dec. 2013.

Robinson, M. C., Morris, K. P., & Dyer, K. R. (1998). Deriving fluxes of suspended particulate matter in the Humber estuary, UK, using airborne remote sensing. *Marine Pollution Bulletin*, *37*, 155-163.

Royal Netherlands Meteorological Institute (KNMI) (2013). Climatology - Daily and hourly weather data of the Netherlands. Available via http://www.knmi.nl/climatology/daily_data/download.html and http://www.knmi.nl/klimatologie/uurgegevens Accessed Dec. 2013.

Rijkeboer, M., Dekker, A.G., & Gons, H.J. (1998). Subsurface irradiance reflectance spectra of inlands waters differing in morphology and hydrology. *Aquatic Ecology*, *31*, 313–323.

Santer, R., & Schmechtig, C. (2000). Adjacency effects on water surfaces: primary scattering approximation and sensitivity study. *Applied Optics*, *39*, 361–375.

Santer, R., Carrère, V., Dessailly, D., Dubuisson, P., & Roger, J-C. (1997). Pixel Identification. *Algorithm Theor. Basis Doc. ATBD 2.17*, Issue 4, Université du

Littoral-Côte d'Opale, Wimereux, F. Available via https://earth.esa.int/instruments/meris/pdf/atbd_2_17.pdf Accessed Dec. 2013

Schroeder, T., Schaale, M., & Fisher, J. (2007). Retrieval of atmospheric and oceanic properties from MERIS measurements: A new Case-2 water processor for BEAM. *International Journal of Remote Sensing*, *28*, 5627–5632.

Shi, W., Wang, M., & Jiang, L. (2011). Spring-neap tidal effects on satellite ocean color observations in the Bohai Sea, Yellow Sea, and East China Sea. *Journal of Geophysical Research-Oceans*, *116*, C12032, doi:10.1029/2011JC007234.

Simpson, J. H., Brown, J., Matthews, J., & Allen, G. (1990). Tidal straining, density currents, and stirring in the control of estuarine stratification. *Estuaries*, *13*, 125–132.

Simpson, J. H., Bos, W.G., Schirmer, F., Souza, A.J., Rippeth, T. P., Jones, S. E., & Hydes, D. (1993). Periodic stratification in the Rhine ROFI in the North Sea. *Oceanologica Acta*, *16*, 23–32.

Sorensen, R. M. (2006). *Basic Coastal Engineering*. Third Edition. New York: Springer. ISBN-10: 0-387-23332-6

Stumpf, R. P., & Werdell P. J. (2010). Adjustment of ocean color sensor calibration through multi-band statistics. *Optics Express*, *18*, 401–412, doi:10.1364/OE.18.000401

Tilstone, G. H., Peters, S. W. M., van der Woerd, H. J., Eleveld, M. A., Ruddick, K., Schönfeld, W., Krasemann, H., Martinez-Vicente, V., Blondeau-Patissier, D., Röttgers, R., Sørensen, K., Jørgensen, P. V., & Shutler, J. D. (2012). Variability in specific-absorption properties and their use in a semi-analytical Ocean Colour algorithm for MERIS in North Sea and Western English Channel coastal waters. *Remote Sensing of Environment*, *118*, 320-338. doi:10.1016/j.rse.2011.11.019

Toffolon, M., Vignoli, G., & Tubino, M. (2006). Relevant parameters and finite amplitude effects in estuarine hydrodynamics. *Journal of Geophysical Research-Oceans*, *111*, C10014, doi:10.1029/2005JC003104.

Uncles, R. J., Lavender, S. J., & Stephens, J. A. (2001). Remotely sensed observations of the turbidity maximum in the highly turbid Humber estuary, UK. *Estuaries, 24*, 745-755.

United States Naval Observatory (USNO) (2013). *US Naval Oceanography Portal. Astromony – Data services – Phases of the Moon – Fraction of the Moon Illuminated*. http://www.usno.navy.mil/astronomy Accessed Dec. 2013.

Valente, A. S., & da Silva, J. C. B. (2009). On the observability of the fortnightly cycle of the Tagus estuary turbid plume using MODIS ocean colour images. *Journal of Marine Systems, 75*, 131-137.

Van der Wal, D., Wielemaker-van den Dool, A., & Herman, P. M. J. (2008). Spatial patterns, rates and mechanisms of saltmarsh cycles (Westerschelde, The Netherlands). *Estuarine Coastal and Shelf Science*, *76*, 357-368

Van der Wal, D., van Kessel, T., Eleveld, M. A., & Vanlede, J. (2010). Spatial heterogeneity in estuarine mud dynamics. *Ocean Dynamics*, *60*, 519–533.

Van der Woerd, H. J., & Pasterkamp, R. (2008). HYDROPT: A fast and flexible method to retrieve chlorophyll-a from multispectral satellite observations of optically complex coastal waters. *Remote Sensing of Environment*, *112*, 1795-1807.

Van der Woerd, H. J., Blauw, A., Peperzak, L., Pasterkamp, R., & Peters, S. (2011). Analysis of the spatial evolution of the 2003 algal bloom in the Voordelta (North Sea). *Journal of Sea Research*, *65*, 195-204.

Van Kessel, T., Vanlede, J., & de Kok, J. (2011). Development of a mud transport model for the Scheldt estuary. *Continental Shelf Research*, *31* (10, Supplement 1), S165-S181.

Vantrepotte, V., Gensac, E., Loisel, H., Gardel, A., Dessailly, V. & Mériaux, X. (2013). Satellite assessment of the coupling between in water suspended particulate matter and mud banks dynamics over the French Guiana coastal domain. *Journal of South American Earth Sciences*, *44*, 25-34.

Verlaan, P. A. J., Donze, M., Kuik, P. (1998). Marine vs Fluvial Suspended Matter in the Scheldt Estuary. *Estuarine, Coastal and Shelf Science*, *46*, 873–883.

Vos, R. J., Hakvoort, J. H. M., Jordans, R. W. J., & Ibelings, B. W. (2003). Multiplatform optical monitoring of eutrophication in temporally and spatially variable lakes. *Science of the Total Environment*, *312*, 221–243.

Werdell, P. J., Franz, B. A., Bailey, S. W., Feldman, G. C., Boss, E., Brando, V. E., Dowell, M., Hirata, T., Lavender, S. J., Lee, Z. P., Loisel, H., Maritorena, S., Mélin, F., Moore, T. S., Smyth, T.J., Antoine, D., Devred, E., Fanton d'Andon, O. H. & Mangin, A. (2013). Generalized ocean color inversion model for retrieving marine inherent optical properties. Applied Optics, 52, 2019-2037.

Table and Figure captions

Table 1

Band settings for the MERIS L2 reflectances.

Table 2

Classification of MERIS images according to semi-diurnal and fortnightly tidal phases, and seasons as a bulk proxy for wind and river discharge.

Table 3

Model simulated geometric mean (and mean) SPM for all conditions in 2006 as a proxy for an unbiased reference set, and model output filtered for clear skies at station VLI, overpass conditions (10:00-11:00 UTC), and both. The latter is a proxy for remotely sensed data. Relative error is the difference between scenario and unbiased reference, relative to the unbiased reference (in percentage).

Fig. 1. Location of the lower estuary (Westerschelde, the Netherlands) and upper estuary (part of the Zeeschelde, Belgium) with distance (in km) from the mouth at Vlissingen. Darker tones in the Westerschelde show deeper areas, a dotted line indicates the thalweg. Used in situ monitoring stations from the MWTL database are indicated as triangles: VLI = Vlissingen, TER = Terneuzen, HOE = Hoedekenskerke, HAN = Hansweert, SCH = Schaar van Ouden Doel. In situ SPM monitoring stations from the NIOZ database (13 in total) are indicated as circles.

Fig. 2. Geometric mean of all independent NIOZ in situ measurements of SPM (mg l^{-1}) versus SPM derived from remote sensing (mg l^{-1}) and the Pearson correlation. y= 1.48x - 0.78 for the arbitrary choice of SPM_{is} as x and SPM_{rs} as y. Root mean square difference (RMSD) following Mélin et al. (2007).

Fig. 3. (a-d) SPM from remote sensing data against semi-diurnal and spring-neap tidal phases for the four main MWTL monitoring stations VLI, TER, HAN and SCH. On the x-axis phase of semi-diurnal tide, in hours before (-) and after (+) HW at the monitoring station, and y-axis shows spring-neap tidal phases, expressed as a factor ranging from 0 (neap tide) to 1 (spring tide). Note that the sun-synchronous satellite samples co-occurrence of low water and spring (x=-5, y=1), and high water and neap (x=1, y=0), at these Westerschelde monitoring stations. Numbers show scaling of the SPM bubbles (in mg l^{-1}). (e-f) Average neap and spring surface current velocity (in m s^{-1}) at these stations as extracted from the Dutch tidal current atlas.

Tidal current conditions that can be sampled by the overpassing satellite are indicated in as black lines.

Fig. 4. Modelled water depth (m, left axis), SPM at the surface (mg l^{-1}, right axis), horizontal flow velocity at the bottom layer (m s^{-1}, right axis) and bottom shear stress (N m^{-2}, right axis). All variables are model results for station TER on 28 and 29 April 2006 (spring tide).

Fig. 5. Geometric mean SPM from in situ stations (symbols) and remote sensing data (lines) along the estuarine thalweg for (a) different semi-diurnal stages, (b) spring and neap conditions, (c) seasons, and (d) geometric mean SPM resulting from North Sea and Westerschelde parameterisation of the retrieval algorithm.

Fig. 6. Composites showing geometric mean SPM for semi-diurnal tides (a) LW, (b) Flood, (c) HW, and (d) Ebb.

Fig. 7. Seasonal composites showing geometric mean SPM for (a) Winter, (b) Spring, (c) Summer, and (d) Autumn.

Table 1

Band settings for the MERIS L2 reflectances.

MERIS band number	Centre wavelength (Spectral bandwidth) in nm
1	412.7 (9.9)
2	442.6 (9.9)
3	489.9 (10.0)
4	509.8 (10.0)
5	559.7 (10.0)
6	619.6 (10.0)
7	664.6 (10.0)
8	680.8 (7.5)
9	708.3 (10)

Table 2

Classification of MERIS images according to semi-diurnal and fortnightly tidal phases, and seasons as bulk proxy for wind and river discharge.

Category	Criteria	Images
Semidiurnal phase	Time (h +HW HAN)	
LW	-6.1 to -4.5, 4.5 to 6.1	29
Flood (incoming)	-4.5 to -1.5	19
HW	-1.5 to +1.5	19
Ebb (outgoing)	+1.5 to +4.5	17
Neap-spring stage	Spring tide fraction	
Neap	0 to 0.25	13
Neap to mean	0.25 to 0.5	19
Mean to spring	0.5 to 0.75	18
Spring	0.75 to 1	34
Season	Month	
Winter	Dec., Jan., Feb. (DJF)	6
Spring	Mar., Apr., May. (MAM)	28
Summer	Jun., Jul., Aug. (JJA)	31
Autumn	Sep., Oct., Nov. (SON)	19

Table 3

Model simulated geometric mean (and mean) SPM for all conditions in 2006 as a proxy for an unbiased reference set, and model output filtered for clear skies at station VLI, overpass conditions (10:00-11:00 UTC), and both. The latter is a proxy for remotely sensed data. Relative error is the difference between scenario and unbiased reference, relative to the unbiased reference (in percentage).

Scenarios	VLI	TER	HOE	HAN	SCH
Unbiased reference	1.33 (28.0)	1.29 (22.2)	1.27 (21.5)	1.25 (20.6)	1.45 (31.3)
No clouds	1.23 (21.8)	1.24 (19.5)	1.22 (19.2)	1.19 (18.1)	1.42 (29.1)
Rel. error	-7.86 (-22.3)	-4.24 (-12.0)	-3.93 (-10.9)	-4.37 (-11.9)	-2.03 (-6.8)
Overpass	1.33 (26.5)	1.32 (23.5)	1.28 (22.3)	1.28 (22.3)	1.48 (33.8)
Rel. error	0.04 (-5.6)	1.92 (6.0)	0.87 (3.5)	2.91 (8.4)	2.16 (8.1)
No clouds at overpass	1.22 (20.4)	1.27 (21.5)	1.23 (20.7)	1.23 (20.8)	1.44 (32.0)
Rel. error	-8.07 (-27.3)	-2.13 (-3.0)	-2.62 (-3.7)	-0.88 (1.3)	-0.38 (2.4)

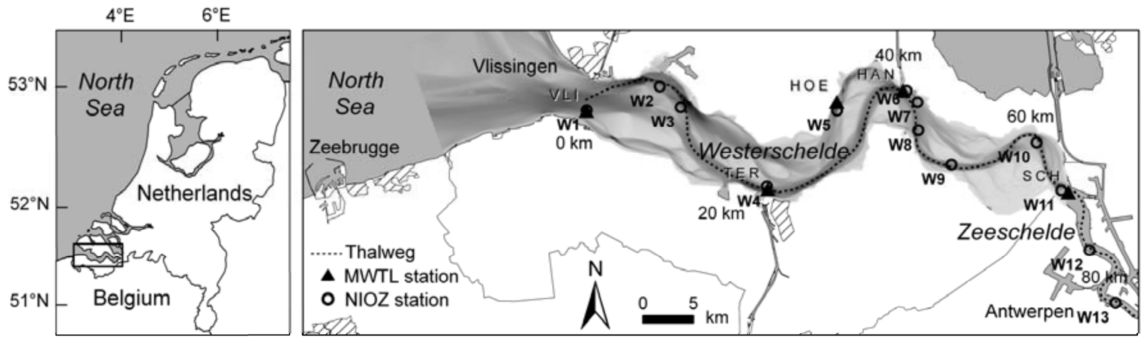

Fig. 1. Location of the lower estuary (Westerschelde, the Netherlands) and upper estuary (part of the Zeeschelde, Belgium) with distance (in km) from the mouth at Vlissingen. Darker tones in the Westerschelde show deeper areas, a dotted line indicates the thalweg. Used in situ monitoring stations from the MWTL database are indicated as triangles: VLI = Vlissingen, TER = Terneuzen, HOE = Hoedekenskerke, HAN = Hansweert, SCH = Schaar van Ouden Doel. In situ SPM monitoring stations from the NIOZ database (13 in total) are indicated as circles.

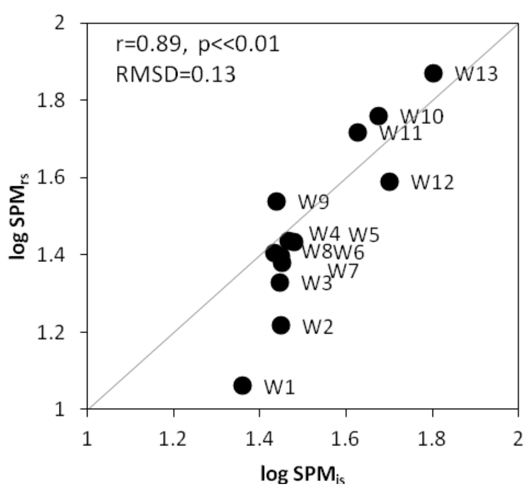

Fig. 2. Geometric mean of all independent NIOZ in situ measurements of SPM (mg l^{-1}) versus SPM derived from remote sensing (mg l^{-1}) and the Pearson correlation. y= 1.48x - 0.78 for the arbitrary choice of SPM_{is} as x and SPM_{rs} as y. Root mean square difference (RMSD) following Mélin et al. (2007).

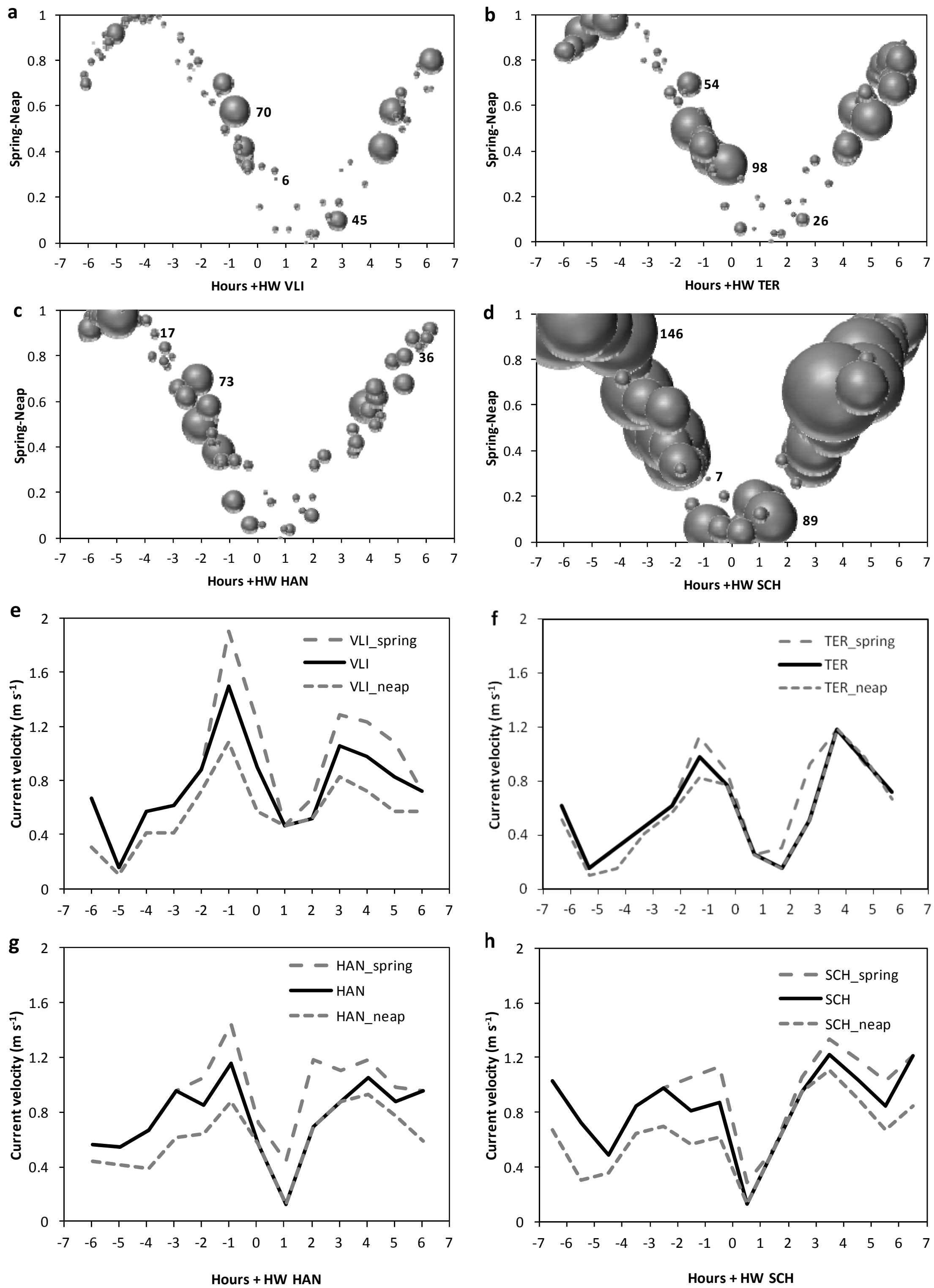

Fig. 3. (a-d) SPM from remote sensing data against semi-diurnal and spring-neap tidal phases for the four main MWTL monitoring stations VLI, TER, HAN and SCH. On the x-axis phase of semi-diurnal tide, in hours before (-) and after (+) HW at the monitoring station, and y-axis

shows spring-neap tidal phases, expressed as a factor ranging from 0 (neap tide) to 1 (spring tide). Note that the sun-synchronous satellite samples co-occurrence of low water and spring (e.g. x=-5, y=1), and high water and neap (x=1, y=0), at these Westerschelde monitoring stations. Numbers show scaling of the SPM bubbles (in mg l^{-1}). (e-f) Average neap and spring surface current velocity (in m s^{-1}) at these stations as extracted from the Dutch tidal current atlas. Tidal current conditions that can be sampled by the overpassing satellite are indicated as black lines.

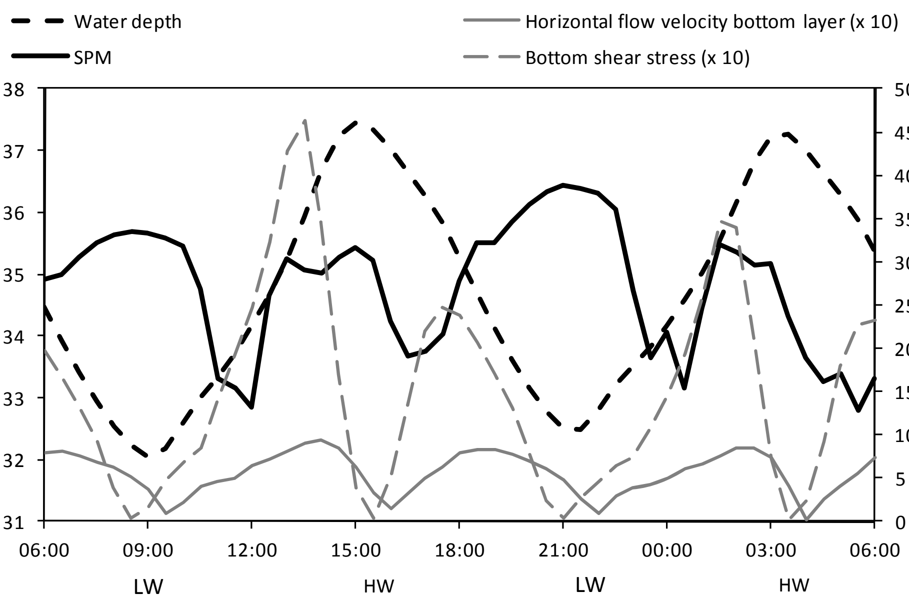

Fig. 4. Modelled water depth (m, left axis), SPM at the surface (mg l^{-1}, right axis), horizontal flow velocity at the bottom layer (m s^{-1}, right axis) and bottom shear stress (N m^{-2}, right axis). All variables are model results for station TER on 28 and 29 April 2006 (spring tide).

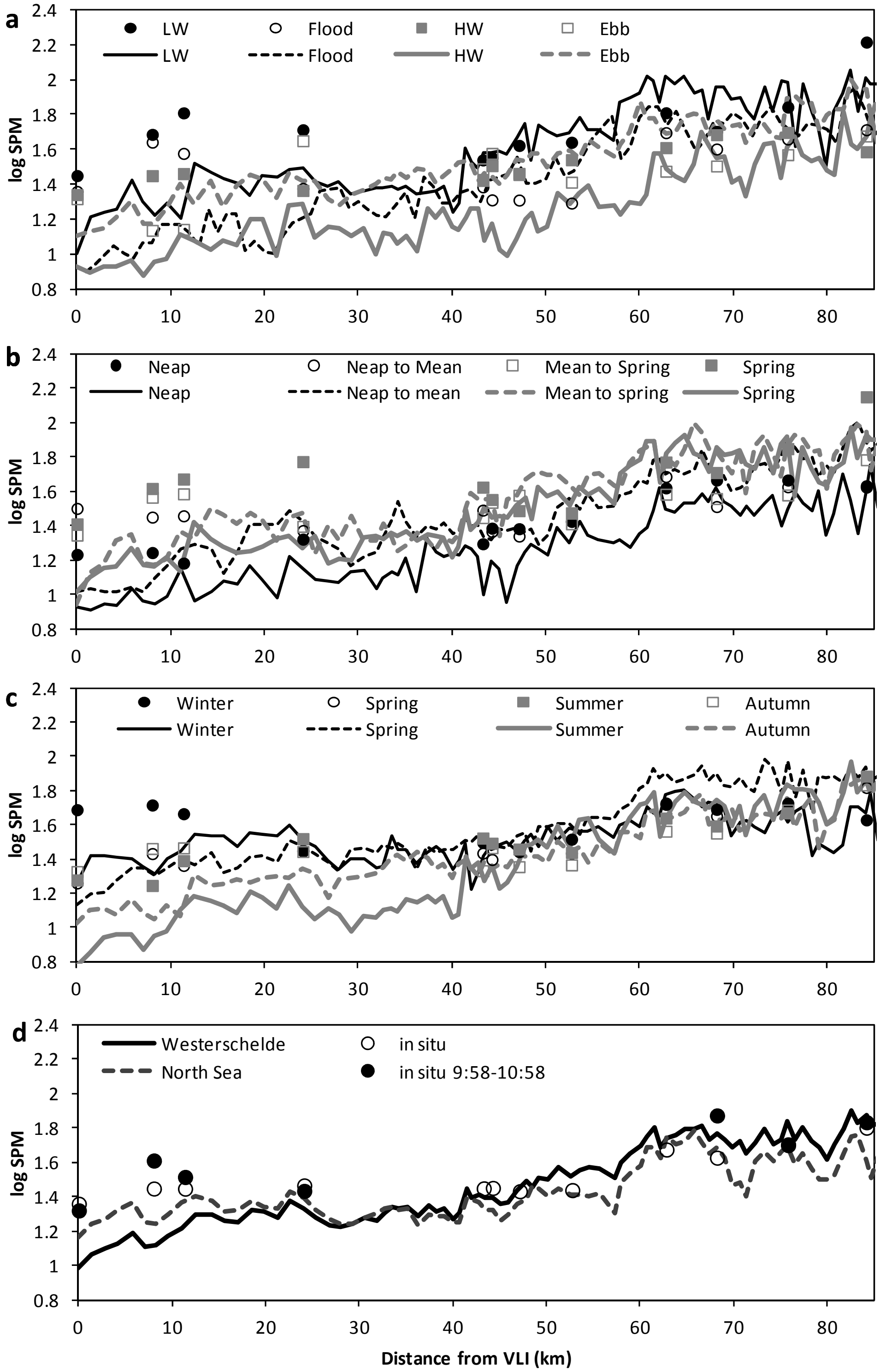

Fig. 5. Geometric mean SPM from in situ stations (symbols) and remote sensing data (lines) along the estuarine thalweg for (a) different semi-diurnal stages, (b) spring and neap conditions, (c) seasons, and (d) geometric mean SPM resulting from North Sea and Westerschelde parameterisation of the retrieval algorithm.

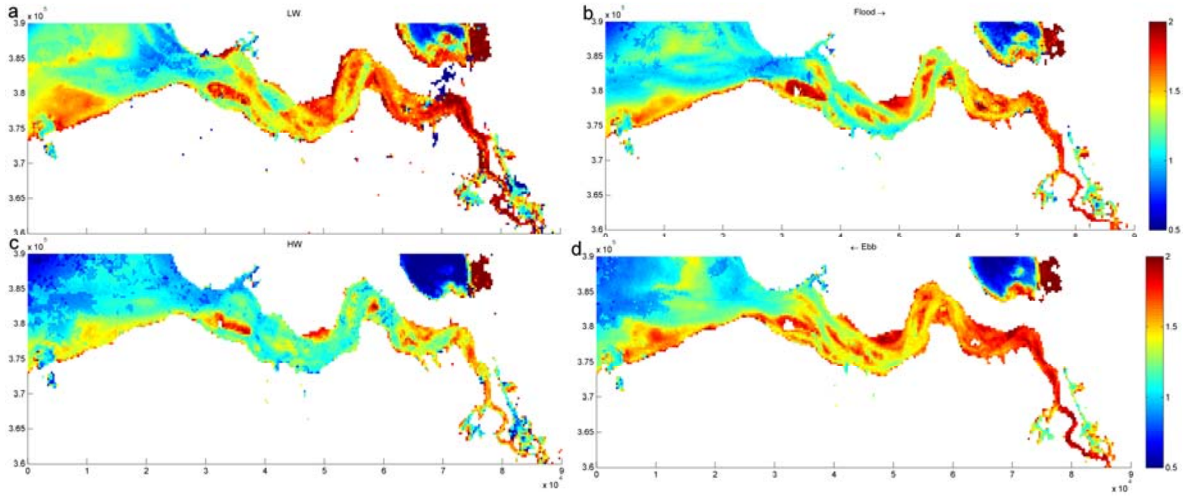

Fig. 6. Composites showing geometric mean SPM for semi-diurnal tides (a) LW, (b) Flood, (c) HW, and (d) Ebb.

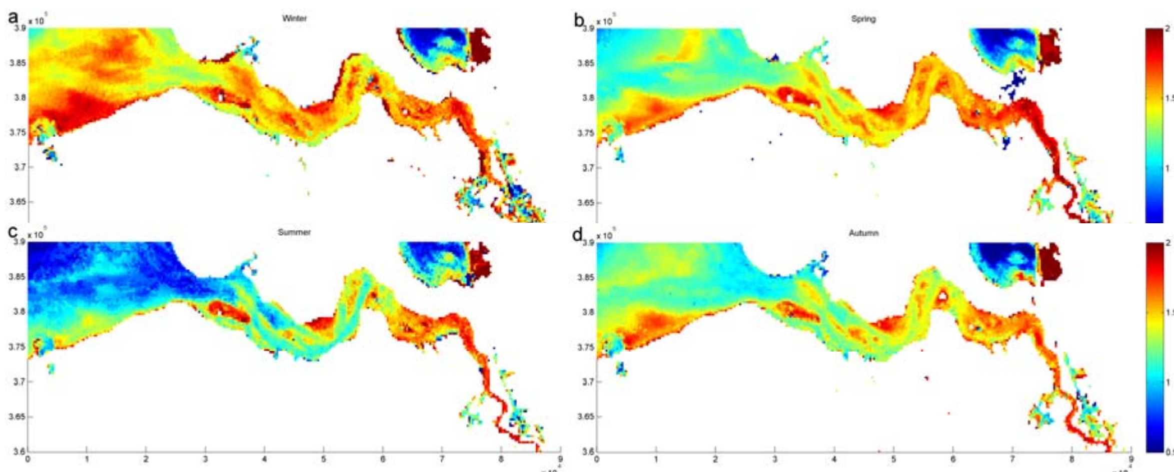

Fig. 7. Seasonal composites showing geometric mean SPM for (a) Winter, (b) Spring, (c) Summer, and (d) Autumn

Electronic supplementary material

Estuarine suspended particulate matter concentrations from sun-synchronous satellite remote sensing: Tidal and meteorological effects and biases

Marieke A. Eleveld, Daphne van der Wal, Thijs van Kessel

Supplementary information detailing the number of images in a cross table (Table S1). Some seasons are better sampled than others, but for every season the distribution of the number of images over the tidal phases is quite similar so that one can safely compare between tidal phases.

Table S1. The contingency tables resulting from the cross tabulations of semi-diurnal tide, and neap-spring tide, for every season.

		Winter	Spring	Summer	Autumn	Total
Nr of images per semi-diurnal tide for every season	LW	3	10	10	6	29
	Flood	2	5	9	3	19
	HW	1	5	7	6	19
	Ebb	0	8	5	4	17
	Total	6	28	31	19	84
Nr of images per neap-spring tide for every season	Neap	1	5	3	4	13
	Neap to mean	1	5	7	6	19
	Mean to spring	1	8	6	3	18
	Spring	3	10	15	6	34
	Total	6	28	31	19	84

Supplementary information showing neap-spring composites (Fig. S1). Due to tidal aliasing, patterns at neap strongly resemble the associated HW composite, while those at spring tide resemble the LW composite. These semi-diurnal composites are presented in Fig. 6 in our article.

a)

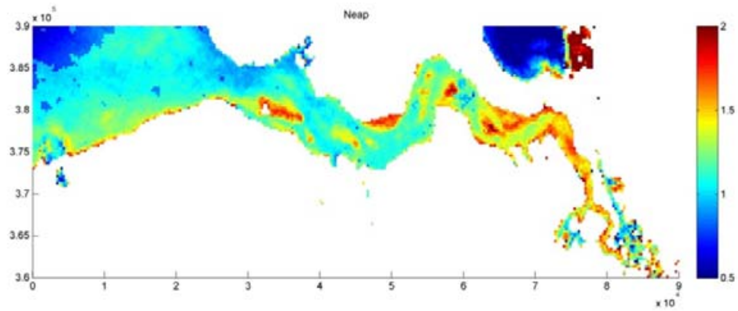

b)

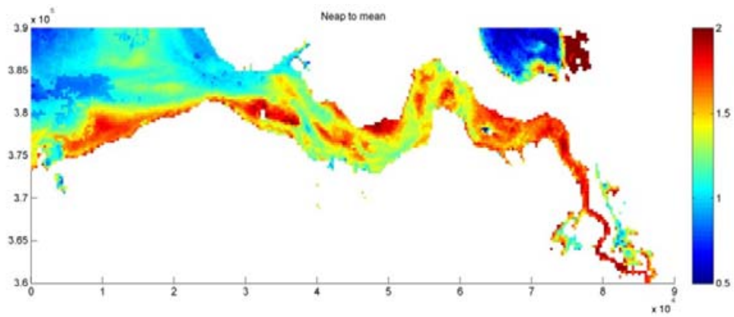

c)

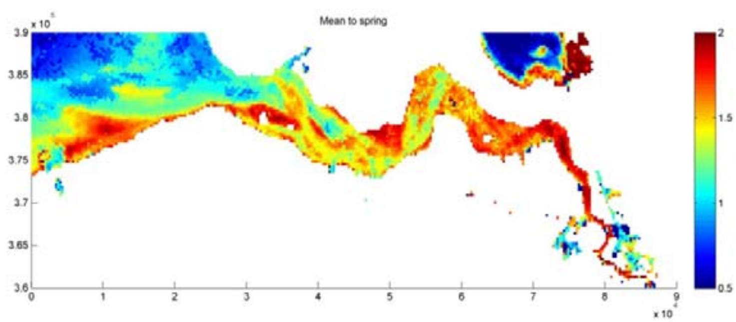

d)

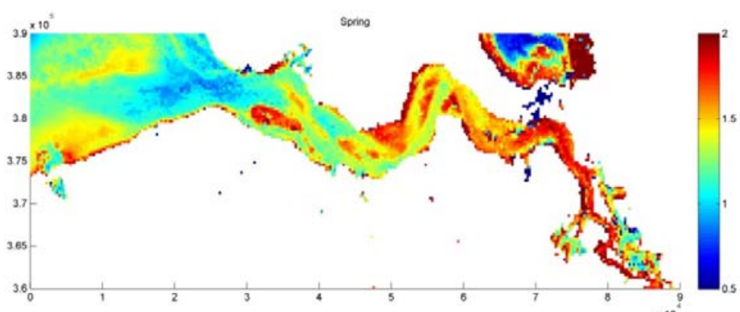

Fig. S1. Neap-spring composites of geometric men SPM for (a) Neap, (b) Neap to mean, (c) Mean to spring, and (d) Spring.

Our KMZ file of the flood composite (Fig 6b) on a Google Earth background.

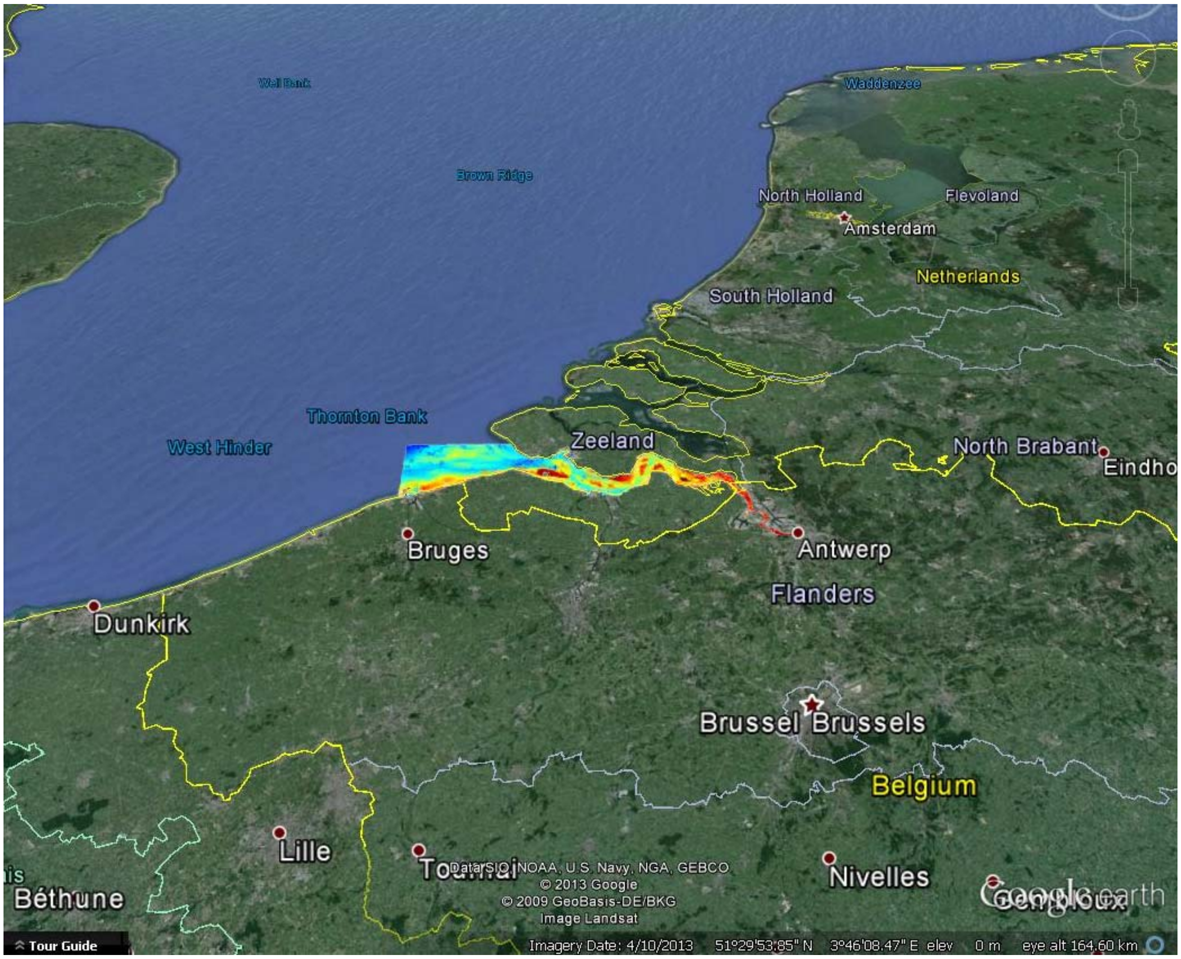

Attribution © Google, Google Earth. Data providers: Data SIO NOAA, U.S. Navy, NGA, GEBCO, © 2013 Google, © 2009 GeoBasis-DE/BKG, Image Landsat